~600 mA/W (@5.5 mW/cm^2) at a bias of 4 V. Intriguingly, they also observed a responsivity of 10 mA/W under the bias-free conditions, which was attributed to the spatial asymmetry electrodes for the imbalanced photocarriers' transport. Later, they presented multi-materials integration by combining perovskite nanocrystals ($CsPbBr_3$) and multilayered graphene, and achieved a high responsivity of 2×10^4A/W (@75 μW/cm^2) with a power detection limit of 10^{-11} W [43]. Xiong et al. [44] reported a graphene–MoS_2–WS_2 heterostructure FPD with a synergetic photogating mechanism, as shown in Figure 1.7a. They found that the photodetectors exhibited an ultrahigh responsivity of ~6.6×10^7 A/W (@6.35 nW/cm^2) and a fast response time of ~7 ms at visible band. Moreover, they revealed that due to the type-II band alignments in MoS_2–WS_2, the photodetectors displayed a responsivity of ~17.1 A/W (@25.4 mW/cm^2) at 1550 nm. Recently, they demonstrated an ultracompact seven-core fiber De-multiplexer by integrating a patterned graphene photodetector array on a single-fiber endface [84], which shows great promise in multicore fiber optics.

In the past years, the figures of merit for fiber photodetectors are significantly improved, benefiting from the heterointegration strategy, as shown in Table 1.1. Nevertheless, the high-speed photodetecting components based on 2D-materials-fiber structure for GHz bandwidth are still lacking until now, which is highly in

Table 1.1 Figures of merit for 2D-materials-fiber photodetectors.

2D-Materials-fiber	V_{ds} (V)	λ (nm)	P (mW/cm^2)	Responsivity (mA/W)	Noise equivalent power (W/Hz$^{1/2}$)	Rise time (ms)	References
Graphene-microfiber	1	1550	9.0×10^6	2.81	~10^{-9}	—	[80]
InSe-microfiber	0.4	543	10–100	769	—	0.045	[81]
CNT/Graphene-DSF	0.3	1550	2.29×10^{-4}	1.48×10^8	6.76×10^{-12}	75	[82]
MoS_2-fiber endface	4	400	5.5	600	—	7.1×10^3	[83]
Graphene-$CsPbBr_3$-fiber endface	0.2	400	7.5×10^{-2}	2×10^7	3.9×10^{-16}	3.1×10^3	[43]
Graphene-MoS_2-WS_2-endface	−3	400	6.35×10^{-6}	6.6×10^{10}	—	7	[44]
		1550	25.4	1.71×10^4	—	10	
Graphene-COF-fiber endface	3	473	3.3×10^{-6}	3.2×10^{10}	~10^{-16}	1.14	[45]
BP-fiber endface	0.5	1550	~79	~8.52×10^3	~1.5×10^{-4}	8×10^{-4}	[47]

demand for the optical communication networks. In another aspect, researchers are exploring the cutting-edge applications of the developed fiber photodetectors. Xiong et al. [45] developed ultrahigh-responsivity photodetectors of 2D covalent organic frameworks (COFs) and graphene with a photoresponsivity of ~3.2×10^7 A/W. Based on the high surface area and the polarity selectivity of COFs, they demonstrated the gas sensing potentials with the fiber phototransitors, as shown in Figure 1.7b. Recently, Xiong et al. [47] for the first time demonstrated twisted BP-based van der Waals stacks for fiber-integrated polarimeters (Figure 1.7c). The real-time in-line detection of the light polarization is crucial in communication, imaging, and sensing fields. The conventional polarimeters use a series of opto-electro-mechanical elements, including lenses, polarizers, waveplates, and photodetectors, which are discretely arranged in an optical path and are highly cumbersome. Recent work ingeniously stacked three photodetection units based on six-layer van der Waals materials, including one isotropic Bi_2Se_3 for power calibration, two twisted BP layers for polarization detection, and three hBN for encapsulation. Intriguingly, the proposed device enabled polarimetric imaging to acquire spatial polarization information by Hadamard single-pixel imaging technique, as shown in Figure 1.7d [47]. The ultracompact device structure with the deterministic and accurate van der Waals materials integration, free from external optical and mechanical modules, may inspire the development of miniaturized optical and optoelectronic systems.

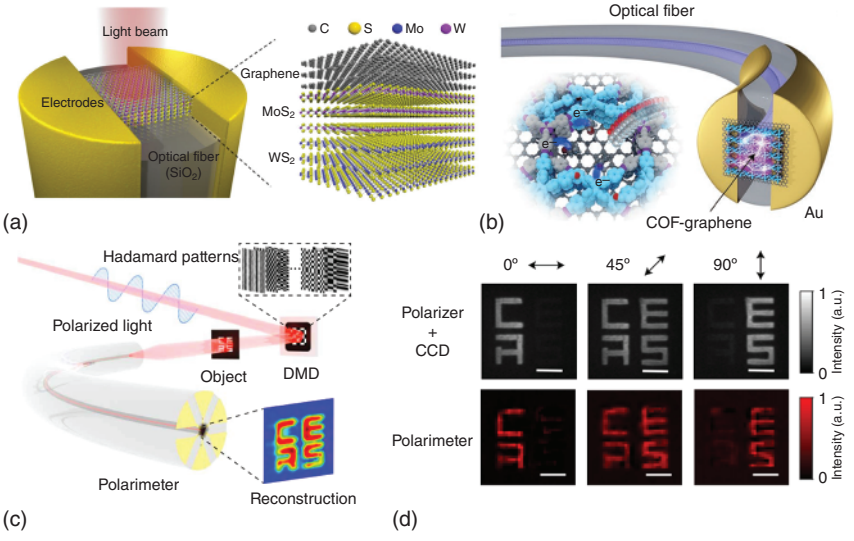

Figure 1.7 Optical fiber photodetectors with 2D-materials integrations. (a) Schematic view of the fiber endface photodetector (FPD) of the graphene-MoS_2-WS_2 heterostructure [44]. (b) Optoelectronic properties of FPD with of the covalent-organic-frameworks (COF) modified graphene film, regulated by gas molecules [45]. (c) Schematic of single-pixel polarimetric imaging by the FPD-based polarimeter. (d) Comparison of the images recorded by the CCD with a polarizer and the images (normalized intensity) reconstructed by the fiber polarimeter device under different linearly polarized illuminations [47]. Scale bars, 1 mm. Source: (a, b) Reproduced with permission from Xiong et al. [44, 45], JOHN WILEY & SONS, INC. (c, d) Reproduced with permission from Xiong et al. [47], American Association for the Advancement of Science - AAAS.

1.2.3.5 Nonlinear Optics

Nonlinear optics is the study of the intense light field in nonlinear media, where the optical response of materials responds nonlinearly to the electric field of light. The optical polarization $\boldsymbol{P}(t)$ of a material to the applied fields can be represented by a power series of the electric field strength $\boldsymbol{E}(t)$, as following:

$$\boldsymbol{P}(t) = \varepsilon_0 \left(\chi^{(1)} \boldsymbol{E}(t) + \chi^{(2)} \boldsymbol{E}(t)^2 + \chi^{(3)} \boldsymbol{E}(t)^3 + \cdots \right) \tag{1.1}$$

where ε_0 is the vacuum permittivity, $\chi^{(n)}$ is the nth order nonlinear susceptibility ($n \geq 2$), and $\chi^{(1)}$ is the linear susceptibility. From Eq. (1.1), it readily indicates that the nonlinear polarization terms can become significant when the light intensity is high. The typical nonlinear optical effects include second-order and third-order nonlinearity, which correspond to the second and third terms in the right side of Eq. (1.1), respectively. From the process of light–matter interactions, the nonlinear effects can also be classified as parametric and nonparametric processes. The parametric process indicates no occurrence of net transfer of energy or momentum between light field and the physical system [85], and it usually includes harmonic generations, sum/difference frequency generation, parametric oscillation, and optical Kerr effect, etc. On the contrast, the nonparametric process indicates that the quantum state of the medium is changed by the process, which includes Raman scattering, Brillouin scattering, two-photon absorption, saturable absorption (SA), and optical limiting, etc. In the past years, there is emerging research interest of 2D-materials nonlinear optics, since they have so many intriguing nonlinear optical properties, such as tunable nonlinearity from stacking order, strain and doping, phase-matching free by the atomic thickness and excitonic resonance [86]. Besides, the nonlinear spectroscopy has been shown to be an effective tool to characterize the fundamental properties of 2D materials. Considering the moderate nonlinear susceptibility of silica materials, for example, the small third-order nonlinearity and zero second-order nonlinearity from centrosymmetry, 2D materials integrations can go beyond the silica fiber nonlinear optics.

The SA is a third-order nonlinear effect of materials, where the light absorption is decreased with increasing light intensity (Figure 1.8a). The SA effect of graphene-based 2D materials has been extensively explored for pulsed fiber lasers spanning the spectra from visible to mid-infrared, along with the *Q*-switched or mode-locked state. In particular, the interplay of broadband gain media, SA effect, and the balance of linear and nonlinear effects in the fiber laser circuit can enable the ultrashort pulse duration. Bao et al. [19] showed that the modulation depth of light absorption could be tuned from 66.5% to 6.2% by varying the graphene layers, as shown in Figure 1.8b. They further reported the use of atomic-layer graphene in a mode-locked fiber laser (Figure 1.8c) for the generation of ultrashort soliton pulses (756 fs) at the telecommunication band. Sun et al. demonstrated a graphene–polymer composite for saturable absorber, and they showed a passively mode-locked fiber laser at 1559 nm, with 5.24 nm spectra bandwidth and ~460 fs pulse duration. Compared with commercial semiconductor saturable absorber mirrors (SESAMs), the graphene is shown to have an ultrawide spectra operation and tunable

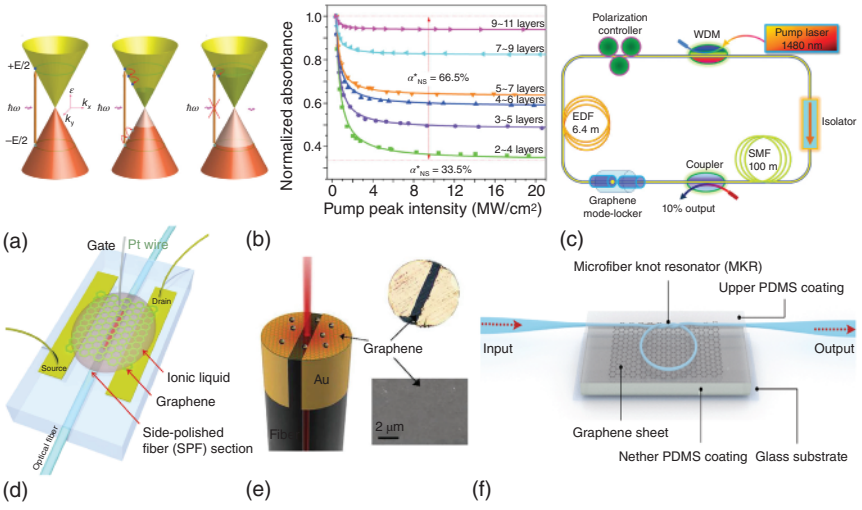

Figure 1.8 Optical fiber integrated with graphene saturable absorber. (a) Schematic of optical interband transition in graphene (left panel), the photogenerated carriers relaxation process (middle panel), and Pauli blocking effect at high excitation intensity (right panel) [19]. (b) Nonlinear absorption of graphene films with different number of layers [19]. (c) Laser configuration constituting a ring cavity. This schematic shows the standard fiber-optic components such as wavelength division multiplexer (WDM), polarization controller, coupler, optical isolator, erbium-doped fiber (EDF), and single-mode fiber (SMF) [19]. (d) Schematic diagram of gate-variable all-fiber graphene device [60]. (e) Schematic of graphene-fiber endface integration device, manipulating by electrical current induced Ohmic heat. Upper right panel shows the microscopic image of the sample. Lower right panel is the scanning electron microscope image of the graphene [87]. (f) Schematic of a high-*Q* microfiber ring resonator (with fiber pigtails) attached to multilayer graphene film and coated by PDMS [88]. Source: (a–c) Reproduced with permission from Bao et al. [19], JOHN WILEY & SONS, INC. (d) Lee et al. [60] / Springer Nature / CC BY 4.0. (e) Reproduced with permission from Li et al. [87], JOHN WILEY & SONS, INC. (f) Reproduced with permission from Ding et al. [89], Elsevier Ltd.

modulation depth, thus the output state of fiber lasers can be dynamically manipulated. Lee et al. [60] reported active control of transmission for graphene–DSF devices with electrical gating (Figure 1.8d), which enabled electrically tunable fiber laser at various operational regimes. Li et al. [87] proposed and demonstrated the state-variable fiber laser by thermally engineering the Fermi–Dirac distributions of graphene films on a fiber endface based on the simple Ohmic heating method, as shown in Figure 1.8e. Similarly, Qin et al. [88] demonstrated tunable laser microcomb dynamics by leveraging the electrical tunability of the graphene device incorporated in a fiber cavity. Recently, Ding et al. [89] realized a multifunctional all-fiber mode-locked laser based on a graphene-integrated polarization-dependent microfiber resonator (Figure 1.8f). They considered the SA mechanism, nonlinear polarization rotation effect, and high-*Q* knot resonator, and observed the *Q*-switched pulse, single soliton mode-locked pulse, harmonic mode-locked pulse, and high-repetition-rate dissipative-FWM pulse depending on the experimental conditions.

Inspired by the graphene research, many other 2D materials, such as BP, TMDCs, and MXenes, are revealed to have SA effect and thus can be used for pulsed fiber lasers. Note that most of the previous work focuses on the spectral and temporal properties (repetition rate and pulse duration) of fiber lasers depending on the various 2D materials and the fiber cavities, while the noise characteristics (intensity noise, timing jitter, and comb-line frequency noise) of the output fiber lasers are less investigated, which is important for optical science and photonic technology [90].

The waveguide-integrated 2D-materials for enhanced parametric processes are attracting attentions, since these nonlinear effects have broad applications in novel light sources, optical sensors, optical metrology, and signal processing. FWM is an intermodulation phenomenon from third-order nonlinearity, and it describes interactions between two and three wavelengths producing two or one new wavelengths. Wu et al. [91] demonstrated the cascaded FWM phenomenon with a large spectral range over 15 nm in a graphene-coated microfiber waveguide. Recently, An et al. [59] reported tunable FWM in graphene–DSF configuration for individual gas molecule detection (Figure 1.9a,b). They showed that the FWM conversion efficiency could change steeply when the graphene Fermi level was tuned approximately at 0.4 eV for ~1.5 μm pump and seed pulse. At this condition, the gas adsorption on graphene with modulated Fermi level would be sensitively detected from the Stokes light signal. SHG is a nonlinear optical process in which two photons with the same frequency are combined to generate a new photon with twice the energy of the initial photons. Chen et al. [52] systematically studied a hybrid WS_2-microfiber structure for broadband and tunable enhancement of light–matter interactions. Based on the high second-order nonlinearity of deposited WS_2, they showed that the SHG conversion in a modified microfiber was ~20 times larger than that of a bare microfiber (surface nonlinearity from symmetry-breaking). They also revealed the strong polarization-dependent SHG of hybrid waveguide due to the interactions between evanescent fields and WS_2, as shown in Figure 1.9c,d. Intriguingly, the dynamic control of SHG by strain gauge was also demonstrated based on the tuning of phase matching (Figure 1.9e), which can be applied for tunable visible light sources. Jiang et al. [92] reported high-efficiency SHG and sum-frequency generation in a microfiber assisted with few-layer GaSe with only submilliwatt continuous-wave pump lasers, and the SHG intensity was enhanced by more than four orders of magnitude. Recently, Li et al. [93] demonstrated deterministic all-optical generation and electrical control of multiple plasmon polaritons in a hybrid graphene-DSF via difference frequency generation. The electrically tunable Fermi level of graphene enables the generation of broadband plasmon polaritons, which provides a new way to high-speed logic operations.

Generally, 2D-material-enhanced optical nonlinearity depends on the trade-off between optical loss and interaction length. The unintentionally generated defects absorption/scattering during 2D materials transfer processes can significantly influence the ultimate nonlinear conversion efficiency in the post-processed fiber devices [10]. Zuo et al. developed a direct growth of MoS_2 onto the internal walls of a silica PCF [62]. By using the as-fabricated 25 cm long fiber, both the SHG and THG

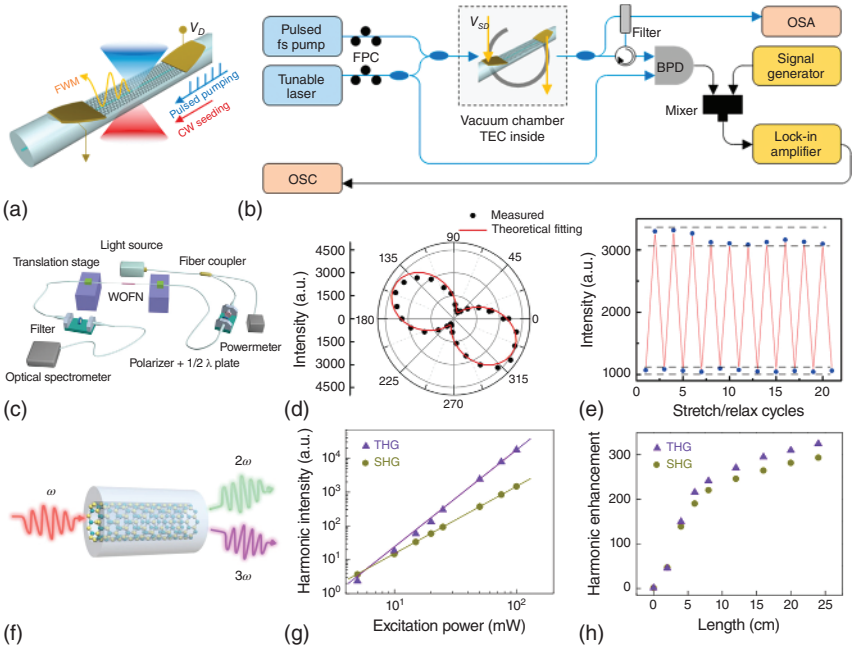

Figure 1.9 Optical fiber integrated with 2D materials for nonlinear optics. (a) Sketch of the electrically tunable four-wave-mixing (FWM) process in graphene–DSF [59]. (b) Experimental setup for gas sensing with based on gate-tunable FWM in graphene. BPD, balanced photodetector; OSA, optical spectrum analyzer; OSC, oscilloscope [59]. (c) Experimental setup for strain control of second harmonic generation (SHG) in the hybrid WS_2-microfiber [52]. WOFN: WS_2 optical fiber nanowire. (d) Polar image of the measured SHG intensity, as a function of the linear polarization of the pump light with a fixed input power [52]. (e) Cycling tests of strain modulation of the SHG of the WS_2-microfiber. Each stretch/relax step corresponds to a strain value of 0.45% [52]. (f) Schematics of SHG (2ω) and third harmonic generation (THG, 3ω) in MoS_2-embedded hollow-core fiber [62]. (g) Excitation-power dependence of SHG and THG intensities for MoS_2-HCF, showing the as-expected quadratic and cubic laws [62]. (h) Fiber-length-dependent SHG and THG enhancements in MoS_2-HCF with respect to MoS_2/silica, showing a general monotonic increase and saturation behavior with the fiber length [62]. Source: (a, b) An et al. [59] / American Chemical Society / CC BY 4.0. (c–e) Chen et al. [52] / Springer Nature / CC BY 4.0. (f–h) Reproduced with permission from Zuo et al. [62], Springer Nature.

were enhanced by ~300 times compared with monolayer MoS_2/silica, as shown in Figure 1.9f–h. This work shows the great potential of mass production of 2D materials fiber devices and can stimulate versatile nonlinear applications in the near future.

1.2.3.6 Fiber-optic Sensors

The fiber-optic sensor uses optical fibers as the sensing element, which exhibits many advantages over the electrical sensors, such as light weight, immune to electromagnetic interference, and remote sensing. In the past years, the 2D-material-integrated fiber-optic sensors attracted research interest, since the photonic/

optoelectronic properties of 2D materials can be strongly modulated by the external stimuli, which can be used to strengthen the performance of the silica fiber-optic sensors. Without loss of generality, here the graphene-based fiber sensors are focused in the scope of chemical and physical sensing, as shown in Table 1.2.

For chemical sensors, the graphene-fiber scheme has appealing features compared with the pure silica fiber structures, since graphene has ultrahigh surface-to-volume ratio, large adsorption capacity, and ultrafast carrier mobility [10, 102]. Generally, the adsorption of molecules changes the dielectric properties of graphene, which indirectly modulated the transported light fields by the amplitude, phase, polarization, or wavelengths. To achieve photonic resonance-enhanced sensing, researchers often integrate the graphene in the evanescent-coupling scheme of DSF, microfibers, gratings, interferometers, and cavities, as shown in Figure 1.10. Wu et al. [94] demonstrated an ultrasensitive gas sensor with a graphene-coated microfiber Bragg grating. They obtained sensitivities of −4 and 2 pm/ppm for NH_3 and xylene gas, respectively, which were 10 times larger than that of a bare microfiber grating. Similarly, Yao et al. [95] reported graphene-enhanced evanescent field in microfiber multimode interferometer (MMF) for gas sensing, and they achieved sensitivities of ~8 pm/ppm (~4 pm/ppm) for NH_3 (H_2O), which were 80 times higher than those of a bare MMF. Xiao et al. [98] studied reduced graphene

Table 1.2 Typical graphene-fiber sensors and their figures of merits.

2D-Materials-fiber	Sensing parameters	Maximal sensitivity	Detection limit	Response time	References
Graphene-microfiber-grating	NH_3	−4 pm/ppm	0.2 ppm	~5 min	[94]
	Xylene	2 pm/ppm	0.5 ppm	~10 min	
Graphene-multimode-microfiber	NH_3	8 pm/ppm	0.1 ppm	~1 s	[95]
	H_2O (vapor)	4 pm/ppm	0.2 ppm		
rGO-microfiber-grating	NO_2	~5 pm/ppm	0.5 ppm	~10 min	[96]
GO-long-period-fiber-grating	NO	~63.6 pm/ppm	0.36 ppm	23.6 min	[97]
Graphene-DSF	Humidity	0.31 dB/%RH	—	~15 s	[98]
Graphene-HCF	Refractive index	365.9 dB/RIU	2.73×10^{-6} RIU	—	[99]
Graphene-fiber-ferrule	Pressure	1.1 nm/Pa	~60 μPa/$Hz^{1/2}$[a]	—	[100]
MoS_2-fiber ferrule	Pressure	89.3 nm/Pa	—	—	[101]
Graphene-etched-fiber-tip	Electrical current	2.2×10^5 nm/A^2	0.3 mA	0.25 s	[48]
Graphene-coiled-microfiber	Electrical current	~6.7×10^4/A^2	0.5 mA	—	[56]

[a] Noise equivalent pressure.

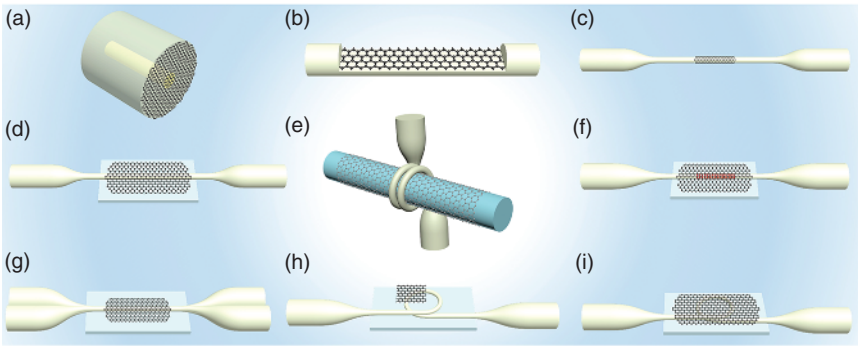

Figure 1.10 Typical optical microstructured fibers integrated with graphene-based 2D materials for sensors. (a–c) Graphene deposited on fiber endface, D-shaped fiber flat surface and tapered microfiber lateral wall. (d–g) Tapered microfiber on graphene substrate, coiled microfiber on graphene-coating rod, microfiber gratings on graphene and microfiber coupler on graphene substrate. (h, i) Microfiber ring partially and fully coated with graphene, respectively.

oxide (rGO)-coated DSF for humidity sensing with a sensitivity of 0.31 dB/% RH (relative humidity) in 75–95% RH (relative humidity). Huang et al. [99] reported plasma-enhanced CVD-growth graphene on hollow-core fibers (HCF), and they obtained a refractive sensitivity of 365.9 dB/RIU and a detection limit of 2.73×10^{-6} RIU. Xu et al. [97] reported ultrasensitive and selective detection of NO gas based on graphene oxide (GO)-coated long-period grating with a sensitivity of 63.6 pm/ppm. They showed that adsorption of NO molecules by GO was the combined effect of physical adsorption and chemical adsorption. In addition to the gases and vapors related sensors, the 2D-materials-fiber-optic sensors have been also implemented for detection of volatile organic compounds and heavy metal ions [103]. Note that there are continuous efforts to improve the chemical sensing sensitivity by optimizing the fiber structures and 2D materials (such as TMDCs, Mxenes, and BP); nevertheless, the sensing performance is fundamentally limited by the simply passive spectral sensing methods.

The active or nonlinear spectral sensing is promising for the ultimate single-molecule detection contributed by the high optical gain and electronic gain technique. Cao et al. [104] reported fluorescent resonance energy transfer in fiber-microfluidic resonator (Figure 1.11a). Besides, by measuring the intermode interference through noise-canceled beat notes and locked-in heterodyne detection with Hz-level precision, they achieved individual molecule sensitivity for dopamine, nicotine, and single-strand DNA detection. Yao et al. [105] demonstrated graphene-enhanced Brillouin optomechanical microresonator for ultrasensitive gas detection (Figure 1.11b,c). Theoretically, the molecular adsorption-induced surface elastic modulation in graphene enabled the Brillouin optomechanical modes extremely sensitive in NH_3 detection. They achieved a detection limit down to 1 ppb and an unprecedented dynamic range over five orders-of-magnitude. Note that the hybrid optical-electronic sensing

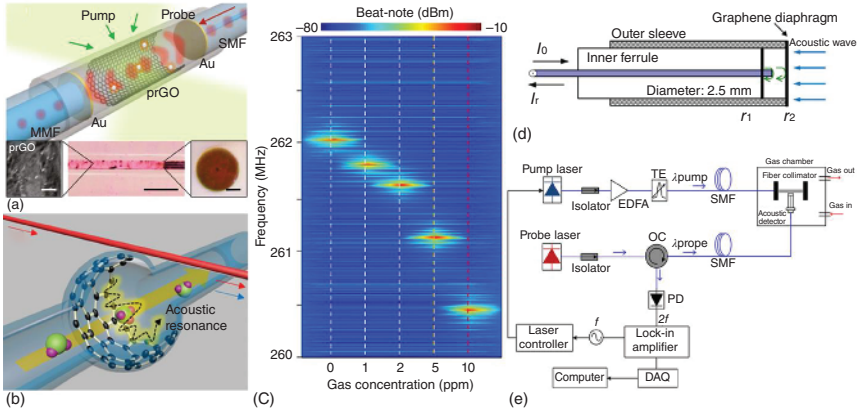

Figure 1.11 Active/nonlinear optical fiber-graphene device for ultrahigh sensitivity sensors. (a) Conceptual design and functionalization of the partially reduced graphene oxide (prGO) inner-deposited fiber sensor [104]. It composes two gold reflectors, prGO deposited inside-fiber, and Rhodamine 6G (Rh6G) as the optical-gain media. Inset from left-to-right shows the scanned electron micrograph of the prGO, the microscopic pictures of the resonator, and the fiber end with Au coverage. Inset scale bars from left-to-right are 2500 and 50 μm, respectively. (b) Schematic of graphene-enhanced Brillouin optomechanics of a microbubble cavity [104]. In this microcavity, the pump mode (red arrow) generates the Stokes mode (blue arrow) and the acoustic mechanical resonance mode (black arrow) [105]. (c) Colored map of the beat note spectra from the cavity optomechanical resonance, varies with the NH_3 gas concentration [104]. (d) Schematic of the fiber Fabry–Pérot interferometer with graphene diaphragm [106]. (e) Setup of photoacoustic spectroscopy system for acetylene detection [105]. Blue line, optical fiber; black line, electrical cable; TF, tunable filter; OC, optical circulator; PD, photo-detector; DAQ, data acquisition; DFB, distributed feedback laser (the pump); ECDL, external-cavity diode laser (the probe); EDFA, erbium-doped fiber amplifier. Source: (a) Cao et al. [104] / Springer Nature / CC BY 4.0. (b, c) Reproduced with permission from Yao et al. [105], American Chemical Society. (d, e) Reproduced with permission from Tan et al. [106], IEEE Publishing.

platform can obtain ultrahigh sensitivity, while the system complexity is also significantly increased compared with the conventional passive sensing methods.

For physical fields sensing, the 2D material-based MEMS are attracting great attention for their supreme optomechanical properties [12]. Ma et al. [49] reported a fiber-tip pressure sensor using a few-layer graphene as a diaphragm (diameter of 25 μm), which formed a low-finesse Fabry–Pérot (FP) interferometer. They realized a high pressure sensitivity over 39.4 nm/kPa. Further, they implemented multilayered graphene as a diaphragm of diameter 125 μm and obtained an improved pressure sensitivity of 1100 nm/kPa. They showed that this kind of graphene-FP cavity could be used for acoustic sensors, exhibiting a flat frequency response in the range of 0.2–22 kHz and a noise-equivalent acoustic single of ~60 $\mu Pa/Hz^{1/2}$ [100]. Later work showed that higher pressure sensitivity was achieved in few-layer MoS_2 diaphragm sensors, probably due to their relatively low Young's modulus of ~0.3 TPa and higher transferred film quality [101]. By integrating the metal electrodes on a fiber endface, Zheng et al. [48] demonstrated a miniature optical fiber current

sensor based on a quasi-static graphene MEMS, and they achieved simultaneously high sensitivity of 2.2×10^5 nm/A^2, a short response time of ~0.25 seconds, and a compact device size of ~15 μm. Besides the quasi-static-response MEMS applications, the intrinsic mechanical resonating properties by the clamped graphene membrane can enable the vibrational fiber-optic sensors for high-precision sensing measurements. For example, Tan et al. [106] reported using a graphene nanomechanical resonator as the acoustic detector, by operating the mechanical resonance of the graphene diaphragm, as shown in Figure 1.11d,e. The sensitivity for acoustic detection was enhanced, and a noise equivalent pressure of 2.11 μPa/Hz$^{1/2}$ was demonstrated. They further presented detection of acetylene gas and achieved a detection limit of 119.8 ppb with 123.9 mW pump power. It is promising to improve the performance of fiber-2D materials-MEMS by optimizing the 2D materials' quality and geometrical structures, and manipulating the pre-stress in fiber devices [10].

1.3 Conclusion

In this chapter, we have reviewed the basic optical properties of several mainstream 2D materials and their integrations to silica optical fibers for advanced optics and optoelectronics applications. We lay emphasis on the optical fiber devices for light field generation, modulation, and detection. Currently, most of the applications remain as proof-of-concept demonstrations, and the issues to realize scalable production with reliable packaging are waiting to be solved before any commercial implement. Recent development of CVD-growth method to produce polycrystalline 2D materials [61, 62], for example graphene and MoS_2 in hollow-core PCF, has provided a unique way to the massive production of hybrid fiber-2D-material devices. As for the future development of fiber-2D-materials integrations, more cutting-edge applications are in demand to explore by merging the extraordinarily properties/functions of 2D materials and the advanced photonic structures. In addition to the classical optics applications, it is very promising to explore the quantum optics in 2D materials for fiber-integrated quantum sources and even the quantum information processing.

References

1 Kao, K.C. and Hockham, G.A. (1966). *Proc. Inst. Electr. Eng.* 113: 1151–1158.
2 Peng, G.-D. (ed.) (2019). *Handbook of Optical Fibers*. Springer.
3 Russell, P. (2003). *Science* 299: 358.
4 Gao, S.-F., Wang, Y.-Y., Ding, W. et al. (2018). *Nat. Commun.* 9: 2828.
5 Brambilla, G., Xu, F., Horak, P. et al. (2009). *Adv. Opt. Photon.* 1: 107.
6 Chen, J.-H., Li, D.-R., and Xu, F. (2019). *J. Lightwave Technol.* 37: 2577.
7 Zhang, L., Tang, Y., and Tong, L. (2020). *iScience* 23: 100810.
8 Abouraddy, A.F., Bayindir, M., Benoit, G. et al. (2007). *Nat. Mater.* 6: 336.
9 Novoselov, K.S., Geim, A.K., Morozov, S.V. et al. (2004). *Science* 306: 666.

10 Chen, J.-H., Xiong, Y.-F., Xu, F., and Lu, Y.-Q. (2021). *Light Sci. Appl.* 10: 78.
11 Dai, Z., Hu, G., Ou, Q. et al. (2020). *Chem. Rev.* 120: 6197.
12 Lee, C., Wei, X., Kysar, J.W., and Hone, J. (2008). *Science* 321: 385.
13 Liu, L., Ryu, S., Tomasik, M.R. et al. (2008). *Nano Lett.* 8: 1965.
14 Neto, A.C., Guinea, F., Peres, N.M. et al. (2009). *Rev. Mod. Phys.* 81: 109.
15 Splendiani, A., Sun, L., Zhang, Y. et al. (2010). *Nano Lett.* 10: 1271.
16 Mak, K.F., He, K., Shan, J., and Heinz, T.F. (2012). *Nat. Nanotechnol.* 7: 494.
17 Li, L., Yu, Y., Ye, G.J. et al. (2014). *Nat. Nanotechnol.* 9: 372.
18 Nair, R.R., Blake, P., Grigorenko, A.N. et al. (2008). *Science* 320: 1308.
19 Bao, Q., Zhang, H., Wang, Y. et al. (2009). *Adv. Funct. Mater.* 19: 3077.
20 Li, W., Chen, B., Meng, C. et al. (2014). *Nano Lett.* 14: 955.
21 Jiang, T., Huang, D., Cheng, J. et al. (2018). *Nat. Photonics* 12: 430.
22 Mak, K.F., Lee, C., Hone, J. et al. (2010). *Phys. Rev. Lett.* 105: 136805.
23 Li, Y., Chernikov, A., Zhang, X. et al. (2014). *Phys. Rev. B* 90: 205422.
24 Xiao, D., Liu, G.-B., Feng, W. et al. (2012). *Phys. Rev. Lett.* 108: 196802.
25 Wen, X., Gong, Z., and Li, D. (2019). *InfoMat* 1: 317.
26 Li, Y., Dong, N., Zhang, S. et al. (2015). *Laser Photonics Rev.* 9: 427.
27 Liu, H., Li, Y., You, Y.S. et al. (2017). *Nat. Phys.* 13: 262.
28 Ling, X., Wang, H., Huang, S. et al. (2015). *Proc. Natl. Acad. Sci.* 112: 4523.
29 Yang, J., Xu, R., Pei, J. et al. (2015). *Light Sci. Appl.* 4: e312.
30 Li, L., Kim, J., Jin, C. et al. (2017). *Nat. Nanotechnol.* 12: 21.
31 Kim, H., Uddin, S.Z., Lien, D.-H. et al. (2021). *Nature* 596: 232.
32 Chen, C., Lu, X., Deng, B. et al. (2020). *Sci. Adv.* 6: eaay6134.
33 Wang, X., Jones, A.M., Seyler, K.L. et al. (2015). *Nat. Nanotechnol.* 10: 517.
34 Biswas, S., Grajower, M.Y., Watanabe, K. et al. (2021). *Science* 374: 448.
35 Wang, X. and Lan, S. (2016). *Adv. Opt. Photon.* 8: 618.
36 Novoselov, K.S., Mishchenko, A., Carvalho, A., and Castro Neto, A.H. (2016). *Science* 353: aac9439.
37 Ma, W., Shabbir, B., Ou, Q. et al. (2020). *InfoMat* 2: 777.
38 Liu, Y., Huang, Y., and Duan, X. (2019). *Nature* 567: 323.
39 Cao, Y., Fatemi, V., Fang, S. et al. (2018). *Nature* 556: 43.
40 Cao, Y., Fatemi, V., Fang, S. et al. (2018). *Nature* 556: 80.
41 Xiong, Y. and Xu, F. (2020). *Adv. Photonics* 2: 064001.
42 Sun, Z., Hasan, T., Torrisi, F. et al. (2010). *ACS Nano* 4: 803.
43 Chen, J.-H., Jing, Q., Xu, F., and Lu, Y.-Q. (2017). *Optica* 4: 835.
44 Xiong, Y.-F., Chen, J.-H., Lu, Y.-Q., and Xu, F. (2019). *Adv. Electron. Mater.* 5: 1800562.
45 Xiong, Y., Liao, Q., Huang, Z. et al. (2020). *Adv. Mater.* 32: 1907242.
46 Wang, H., Xiong, Y., Wu, C. et al. (2022). *Opt. Express* 30: 6818.
47 Xiong, Y., Wang, Y., Zhu, R. et al. (2022). *Sci. Adv.* 8: eabo0375.
48 Zheng, B.-C., Yan, S.-C., Chen, J.-H. et al. (2015). *Laser Photonics Rev.* 9: 517.
49 Ma, J., Jin, W., Ho, H.L., and Dai, J.Y. (2012). *Opt. Lett.* 37: 2493.
50 Luo, Z.-C., Liu, M., Guo, Z.-N. et al. (2015). *Opt. Express* 23: 20030.
51 Chen, J.-H., Luo, W., Chen, Z.-X. et al. (2016). *Adv. Opt. Mater.* 4: 853.
52 Chen, J.-H., Tan, J., Wu, G.-X. et al. (2019). *Light Sci. Appl.* 8: 8.

53 Chen, J.-H., Zheng, B.-C., Shao, G.-H. et al. (2015). *Light Sci. Appl.* 4: e360.
54 Xu, F., Horak, P., and Brambilla, G. (2007). *Opt. Express* 15: 7888.
55 Kou, J.-L., Chen, J.-H., Chen, Y. et al. (2014). *Optica* 1: 307.
56 Yan, S.-C., Zheng, B.-C., Chen, J.-H. et al. (2015). *Appl. Phys. Lett.* 107: 053502.
57 Li, C., Chen, J., Yan, S. et al. (2016). *IEEE Photon. J.* 8: 1500307.
58 Zhang, H., Healy, N., Shen, L. et al. (2016). *Sci. Rep.* 6: 23512.
59 An, N., Tan, T., Peng, Z. et al. (2020). *Nano Lett.* 20: 6473.
60 Lee, E.J., Choi, S.Y., Jeong, H. et al. (2015). *Nat. Commun.* 6: 6851.
61 Chen, K., Zhou, X., Cheng, X. et al. (2019). *Nat. Photonics* 13: 754.
62 Zuo, Y., Yu, W., Liu, C. et al. (2020). *Nat. Nanotechnol.* 15: 987.
63 Bao, Q., Zhang, H., Wang, B. et al. (2011). *Nat. Photonics* 5: 411.
64 Kim, J.T. and Choi, C.-G. (2012). *Opt. Express* 20: 3556.
65 Zhang, H., Healy, N., Shen, L. et al. (2016). *J. Lightwave Technol.* 34: 3563.
66 Chu, R., Guan, C., Yang, J. et al. (2017). *Opt. Express* 25: 13278.
67 Cui, Y., Lu, F., and Liu, X. (2017). *Sci. Rep.* 7: 40080.
68 Schell, A.W., Takashima, H., Tran, T.T. et al. (2017). *ACS Photonics* 4: 761.
69 Liao, F., Yu, J., Gu, Z. et al. (2019). *Sci. Adv.* 5: eaax7398.
70 Toth, M. and Aharonovich, I. (2019). *Annu. Rev. Phys. Chem.* 70: 123.
71 Aharonovich, I., Englund, D., and Toth, M. (2016). *Nat. Photonics* 10: 631.
72 He, Y.-M., Clark, G., Schaibley, J.R. et al. (2015). *Nat. Nanotechnol.* 10: 497.
73 Yu, S., Wu, X., Wang, Y. et al. (2017). *Adv. Mater.* 29: 1606128.
74 Liu, Z.-B., Feng, M., Jiang, W.-S. et al. (2013). *Laser Phys. Lett.* 10: 065901.
75 Yu, S., Wu, X., Chen, K. et al. (2016). *Optica* 3: 541.
76 Gan, X., Zhao, C., Wang, Y. et al. (2015). *Optica* 2: 468.
77 Xu, K., Xie, Y., Xie, H. et al. (2018). *J. Lightwave Technol.* 36: 4730.
78 Dong, L., Liu, X., Zhang, Y. et al. (2020). *ACS Appl. Electron. Mater.* 2: 447.
79 Cheng, X., Zhou, X., Tao, L. et al. (2020). *Nanoscale* 12: 14472.
80 Sun, X., Qiu, C., Wu, J. et al. (2015). *Opt. Express* 23: 25209.
81 Jin, Z., Ye, F., Zhang, X. et al. (2018). *ACS Nano* 12: 12571.
82 Zhuo, L., Fan, P., Zhang, S. et al. (2020). *Nanoscale* 12: 14188.
83 Chen, J.-H., Liang, Z.-H., Yuan, L.-R. et al. (2017). *Nanoscale* 9: 3424.
84 Xiong, Y., Xu, H., Wang, Y. et al. (2022). *ACS Photonics* 9: 1808.
85 Boyd, R.W. (2020). *Nonlinear Optics*. Academic Press.
86 Autere, A., Jussila, H., Dai, Y. et al. (2018). *Adv. Mater.* 30: 1705963.
87 Li, C., Chen, J.-H., Wang, W.-S. et al. (2017). *Adv. Opt. Mater.* 5: 1700630.
88 Qin, C., Jia, K., Li, Q. et al. (2020). *Light Sci. Appl.* 9: 185.
89 Ding, Z.-X., Chen, Y., and Xu, F. (2021). *Opt. Laser Technol.* 143: 107381.
90 Kim, J. and Song, Y. (2016). *Adv. Opt. Photonics* 8: 465.
91 Wu, Y., Yao, B.C., Feng, Q.Y. et al. (2015). *Photonics Res.* 3: A64.
92 Jiang, B., Hao, Z., Ji, Y. et al. (2020). *Light Sci. Appl.* 9: 63.
93 Li, Y., An, A., Lu, Z. et al. (2022). *Nat. Commun.* 13: 3138.
94 Wu, Y., Yao, B., Zhang, A. et al. (2014). *Opt. Lett.* 39: 1235.
95 Yao, B.C., Wu, Y., Zhang, A.Q. et al. (2014). *Opt. Express* 22: 28154.
96 Sridevi, S., Vasu, K., Bhat, N. et al. (2016). *Sens. Actuators, B* 223: 481.
97 Xu, B., Huang, J., Xu, X. et al. (2019). *ACS Appl. Mater. Interfaces* 11: 40868.

98 Xiao, Y., Zhang, J., Cai, X. et al. (2014). *Opt. Express* 22: 31555.
99 Huang, M., Yang, C., Sun, B. et al. (2018). *Opt. Express* 26: 3098.
100 Ma, J., Xuan, H., Ho, H.L. et al. (2013). *IEEE Photon. Technol. Lett.* 25: 932.
101 Yu, F., Liu, Q., Gan, X. et al. (2017). *Adv. Mater.* 29: 1603266.
102 Shivananju, B.N., Yu, W., Liu, Y. et al. (2017). *Adv. Funct. Mater.* 27: 1603918.
103 Pawar, D. and Kale, S.N. (2019). *Microchim. Acta* 186: 253.
104 Cao, Z., Yao, B., Qin, C. et al. (2019). *Light Sci. Appl.* 8: 107.
105 Yao, B., Yu, C., Wu, Y. et al. (2017). *Nano Lett.* 17: 4996.
106 Tan, Y., Zhang, C., Jin, W. et al. (2017). *IEEE J. Sel. Top. Quantum Electron.* 23: 199.